Carbon Capture Science & Technology 9 (2023) 100138

Contents lists available at ScienceDirect

Carbon Capture Science & Technology

journal homepage: www.elsevier.com/locate/ccst

Full Length Article

Combining machine learning with multi-physics modelling for multi-objective optimisation and techno-economic analysis of electrochemical CO_2 reduction process

Lei Xing[a,*], Hai Jiang[b], Xingjian Tian[b], Huajie Yin[c], Weidong Shi[b], Eileen Yu[d], Valerie J. Pinfield[d], Jin Xuan[a]

[a] School of Chemistry and Chemical Engineering, University of Surrey, Guildford GU2 7XH, UK
[b] School of Chemistry and Chemical Engineering, Jiangsu University, Zhenjiang 212013, China
[c] Institute of Solid State Physics, Hefei Institute of Physical Science, Chinese Academy of Sciences, Hefei 230031, China
[d] Department of Chemical Engineering, Loughborough University, Loughborough LE11 3TU, UK

A R T I C L E I N F O

Keywords:
Electrochemical CO_2 reduction
Gas diffusion electrode
Multi-physics modelling
Machine learning
Multi-objective optimisation

A B S T R A C T

As a carbon capture and utilization (CCU) technology, gas diffusion electrode (GDE) based electrochemical CO_2 reduction reaction (eCO_2RR) can convert CO_2 to valuable products, such as formate and CO. However, the electrode parameters and operational conditions need to be studied and optimised to enhance the performance and reduce the net cost of the eCO_2RR process before its industrial application. In this work, a machine learning algorithm, i.e., extended adaptive hybrid functions (E-AHF) is combined with a multi-physics model for the data-driven three-objective optimisation and techno-economic analysis of the GDE-based eCO_2RR process. The effects of eight design variables on the product yield (PY), CO_2 conversion (CR) and specific electrical energy consumption (SEEC) of the process are analysed. The results show that the R^2 of the E-AHF model for the prediction of PY, CR and SEEC are all higher than 0.96, indicating the high accuracy of the developed machine learning algorithm for the prediction of the eCO_2RR process. The process performance experiences a notable improvement after optimisation and is affected by a combination of eight variables, amongst which the electrolyte concentration having the most significant impact on PY and CR. The optimal trade-off single-pass PY, CR and SEEC are 3.25×10^{-9} kg s^{-1}, 0.663% and 9.95 kWh kg^{-1} based on flow channels with 1 cm in length, respectively. The SEEC is reduced by nearly half and PY and CR are improved more than two times after optimisation. The production cost of the GDE-based eCO_2RR process was approximately \$378 t^{-1}product (CO and formate), much lower than that of traditional CO_2 utilisation factories (\$835 t^{-1}product). The electricity cost accounted for more than 80% of the total cost, amounting to \$318 t^{-1}, indicating that cheaper and cleaner electricity sources would further reduce the production cost of the process, which is the key to the economics of this technology.

1. Introduction

CO_2 reduction through electrochemical route is one of the CO_2 capture and utilisation (CCU) technologies (Budzianowski, 2012), which can convert CO_2 into value-added raw materials and chemical products, such as CO, syngas, formate ($HCOO^-$), methane (CH_4) and ethyl alcohol (C_2H_5OH) (Yamamoto et al., 2002; Hori et al., 1994; Ogura, 2013). With renewable and carbon-neutral energy sources, electrochemical reduction of CO_2 can be one of the negative emissions technology (NET), which can convert intermittent and unstable energy (i.e., solar and wind) to stable chemical form for further storage and utilisation (Whipple and Kenis, 2010). Currently, the most significant limitation of the electrochemical CO_2 reduction process is the low current density, which is mainly caused by the low CO_2 mass transfer rate and the reduction reaction rate (Xiang et al., 2019; Nguyen and Dinh, 2020; García de Arquer et al., 2020), which strongly limit the practical application of eCO_2RR technology. To break the limitation, intensive research has been concentrated on the development of high-performance electrodes and catalysts to improve the CO_2 reduction efficiency and the product yield (García de Arquer et al., 2020). Higuchi et al. (2018) used the modified Bönnemann method to prepare Pt_xRu (x = 1, 3, and 4) alloy-loaded carbon black (Pt_xRu/C) catalysts, which achieved 91.7% faraday efficiency (EF) in methylcyclohexane production from CO_2. Kwok et al. (2019) designed a kind of nano-folded gold catalyst for the eCO_2RR system and indicated that the FE of CO production was about 87.4%.

* Corresponding author.
E-mail address: l.xing@surrey.ac.uk (L. Xing).

https://doi.org/10.1016/j.ccst.2023.100138
Received 5 August 2023; Received in revised form 6 September 2023; Accepted 7 September 2023

In addition to high-performance catalysts, the configuration of the electrolyser also plays a crucial role in enhancing the reaction surface area and promoting the mass transport rate. The gas diffusion electrode (GDE)-based electrolyser is a more advanced design that tends to be used in eCO_2RR systems due to the potential performance improvement under mild operating conditions (i.e., ambient pressure and room temperature) (Nguyen and Dinh, 2020; Lu et al., 2014). The porous catalyst layer (CL) in the GDE is the predominant location of the electrochemical reactions, thus enlarging the specific area of reaction, alleviating the CO_2 mass transfer resistance and shortening the distance travelled by the reactants to the reaction sites (Liang et al., 2020; De Mot et al., 2019; Tan et al., 2020). Weng et al. (2018) developed a physics-based model to simulate the CO_2 reduction inside the GDE. The results confirmed that the CO_2 conversion efficiency is highly limited by the CO_2 mass transfer and it can be improved significantly by implementing porous CL. Blake et al. (2021) compared the CO_2 reduction performance of a GDE-based planar electrode through modelling, which indicated that the GDE can improve the diffusivity and solubility of CO_2 in water and facilitate current densities orders of magnitude higher than the limiting current densities of the traditional planar electrodes. Recently, several studies have been published focusing on the effect of different parameters in GDE. The studies of Yang et al. (2021a) revealed the significant effect of the cell potential on the performance of GDE, in which the results indicated that the cell potential affected the wetting characteristics of the hydrophobic gas diffusion layer (GDL), resulting in flooding that further lowers the stability of the GDE during operation Petrov et al. (2022) developed a model for the water transport through the AEM during electrochemical CO_2 reduction process with micro-channels in CL accounting for the crossover of $K+$ and AEM conductivity, which revealed that membrane with channels of promise geometry can increase the current density by up to 40% compared to a traditional AEM. Yang et al. (2021c) studied five parameters, i.e., applied cathode potential, catalyst loading, porosity, inlet gas composition and velocity, based on a two-dimensional steady-state multiphase GDE model, which showed that 0.5 M KOH catholyte at the volumetric velocity of 0.5 mL min^{-1} is a relatively optimised working condition. Weng et al. (2019b) compared aqueous GDE, full-MEA and exchange MEA through a physical-based model, in which several operation conditions were determined for the optimal working ranges of different types of configurations. The system with the 0.5 M KOH catholyte and at the volumetric flowrate of 0.5 mL min^{-1} is selected as it could generate a higher current density and more formate under the same applied cathode potential, without contamination of C2 products.

To date, most research on eCO_2RR process and system is dedicated to developing stable, efficient, and selective catalysts through experimentation or physics-based modelling (García de Arquer et al., 2020). Limited attention has been paid to the optimisation of electrode parameters and operational conditions (Gabardo et al., 2019) and even fewer studies focus on the integration of mechanistic physics-based simulations and data-driven surrogate models. Currently, there have been some physics-based models for simulating the GDE system (Wu et al., 2015; Wang et al., 2013; Li and Oloman, 2007), but these are restricted by the complex process for solving partial differential equations (PDEs) over a complex geometry and the computational and time costs are still unaffordable for further multi-variable and multi-objective optimisation. Machine-learning, algorithm-based, data-driven surrogate models, the simplified alternative of the original mechanistic models, are considered to be a promising approach to investigate multi-variable and multi-objective optimisation problems (Jiang et al., 2023). There are already some data-driven surrogate models used for optimisation of systems, e.g., response surface methodology (RSM) (Xing et al., 2023), Kriging (KRG) (Bouhlel and Martins, 2019), recurrent neural networks (RNN) (Lei et al., 2023) and artificial neural networks (ANN) (Wang et al., 2023; Sun et al., 2005). These individual algorithms have different strengths and weaknesses. For instance, RSM and KRG are statistic-based approaches, mainly focus on regression and can achieve relatively high accuracy with a relatively simple algorithms and low requirement of massive training data, but less suitability for the multi-variables optimisation problems (Sun et al., 2005). RNN and ANN are two different neural networks frequently used in deep learning, mainly focusing on feature extraction and classification, which are entirely data driven without prior knowledge of the statistics of the problems and data. They are potentially extendable more readily to large numbers of variables and normally able to predict objectives more accuracy with the support of big data. Surrogate modelling packages and toolboxes were also developed, e.g., the surrogate modelling toolbox (SMT) developed by Saves et al. (2023) and the object-orientated derivative-free optimisation (OODX) developed by Durkin and Guo (2023) as an open-source Python package. To trade off the complexity and accuracy of various data driven approaches, an extended adaptive hybrid functions (E-AHF) (Xing et al., 2023; Saves et al., 2023), an advanced machine learning algorithm, is adopted as the data-driven surrogate model in this work for the multi-variable and multi-objective optimisation of the eCO_2RR system. The E-AHF model improves prediction accuracy by utilising the advantages of multiple individual machine learning algorithms and selecting the best combination of them at each data point (Jiang et al., 2023; Song et al., 2018). Some work has already been reported on combined machine learning and physics-based models to optimise CCU technology (Xing et al., 2023; Lei et al., 2023), but few concentrated on the GDE-based eCO_2RR systems. In addition to the optimisation of performance, techno-economic analysis (TEA) of the technology is critical before industrial application (Hossain et al., 2019). While there have been some evaluations of the TEA of CO_2 utilisation systems in previous studies (De Luna et al., 2019; Pérez-Fortes et al., 2016), there is a lack of research on the TEA specifically for the GDE-based eCO_2RR system. The objective of this study is to address this knowledge gap to some extent.

In this work, a physics-based mechanistic model is integrated with machine-learning-based surrogate approaches to conduct multi-objective optimisation and techno-economic analysis of a GDE-based eCO_2RR process. Firstly, a two-dimensional, multi-phase flow, multi-physics, isothermal model was developed to describe the detailed electrochemical and physical processes occurred within the GDE-based CO_2 electrolyser. After experimental validation, the mechanistic model was used to generate data for training the E-AHF surrogate model. The prediction accuracy of the E-AHF models was evaluated by R-squared (R^2) and relative error. The nondominated sorting genetic algorithm II (NSGA-II) was applied for the multi-objective optimisation. Three electrode parameters, i.e., porosity, electrolyte channel width, and catalyst loading, and five operating conditions, i.e., cathode potential, feed gas velocity, electrolyte concentration, electrolyte flow velocity, and inlet mole fraction of CO_2, were investigated and optimised for the trade-off of three objective functions, i.e., product yield, CO_2 conversion and reduced energy consumption. Finally, based on the optimal trade-off results, the TEA of the optimal process was performed. The simulation approach developed in this work is also suitable in studying and optimising other complex electrochemical processes beyond the GDE-based eCO_2RR process.

2. Methodology

2.1. Physics-based mechanistic model

A two-dimensional, multiphase, multi-physics, isothermal model of the GDE-based microfluidic electrochemical CO_2 reduction process is established in this work. As shown in Fig. 1, the model focuses on the entire electrolyser, consisting of the electrolyte channel (ELEC), anode catalyst layer (ACL) at the anode side, the gas chamber (GASC), gas diffusion layer (GDL), and the cathode catalyst layer (CCL) at the cathode side, and an alkaline exchange membrane (MEM) in between. In this model, the GDL is treated to be a single-layer porous and hydrophobic medium (Nguyen and Dinh, 2020) and the CL is assumed to be a porous substance containing numerous cylinder-shaped parallel chan-

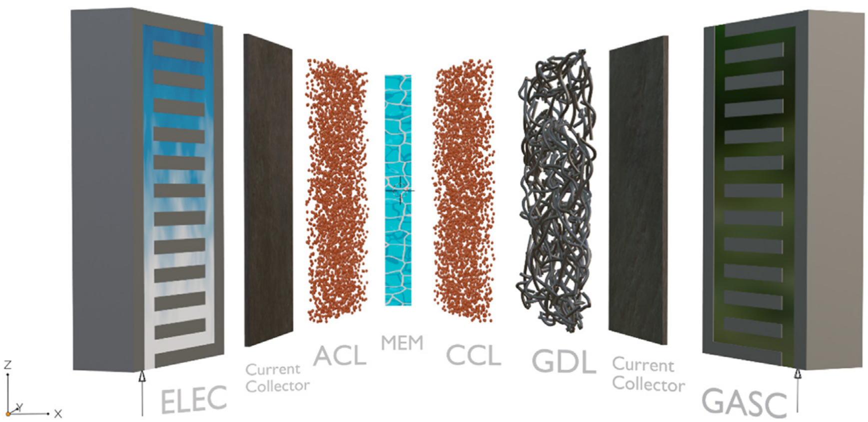

Fig. 1. Schematic configuration of the GDE-based microfluidic CO_2 electrolyser.

nels and the Cu_xO granular catalyst particles (a mixture of Cu_2O, CuO, and Cu) are coated on the inner surface of the channels (Ma et al., 2016; Yang et al., 2021b). The electrolyte (potassium hydroxide, KOH) and the aqueous products flow through the ELEC. The mixed gas (CO_2 and N_2) is directly fed into the GASC and diffuses through the GDL into the CCL. The CO_2 electrochemical reduction reactions occur inside the CCL, converting CO_2 into various products (CO and formate). The geometrical parameters in our model are listed in Table S1 in the supplementary information (SI). The model takes into account the CO_2 mass transport, species distributions and multiple competing reaction pathways. The governing equations that describe these processes are presented in the subsequent sections.

2.1.1. Charge transfer reactions

Two competing CO_2 electrochemical reduction reactions occurring in the CL are shown as follows:

$$CO_2(aq){+}H_2O + 2e^- \leftrightarrow HCOO^-{+}OH^- \tag{1}$$

$$CO_2(aq){+}H_2O + 2e^- \leftrightarrow CO + 2OH^- \tag{2}$$

Through reactions (1) and (2), CO_2 can be reduced to formate and CO respectively. It is worth noting that besides the above reactions, an undesirable hydrogen evolution reaction (HER) occurs in the CCL simultaneously. The HER in alkaline conditions is expressed as:

$$2H_2O + 2e^- \leftrightarrow H_2{+}2OH^- \tag{3}$$

2.1.2. Transport of gaseous species

Gaseous species, including $CO_{2(g)}$, N_2, H_2 and CO, are considered in the GASC, the GDL and the CL. The mass conservation of gaseous species is described by the following expression (Bongers and De Goey, 2003; Weng et al., 2020):

$$\nabla \cdot \left(-\rho_g D_{i,m} \nabla \omega_i - \rho_g \omega_i D_{i,m} \frac{\nabla M_g}{M_g} \right) + \nabla \cdot \left(\rho_g u_g \omega_i \right) = R_{i,m} \tag{4}$$

where i denotes the gaseous species, ρ_g represents the mixture gas density, ω_i denotes the mass fraction of the gaseous species, M_g is the averaged molar weight of the gas mixture, $D_{i,m}$ is the diffusivity of each gaseous species and u_g is mixture gas velocity, and $R_{i,m}$ is the source term of each species, which is zero in the GASC and GDL. The source term in the CL can be found in Table S2 of the SI.

In the GASC, the diffusivity, $D_{i,m}$, is derived from the Maxwell-Stefan equation and simplified by assuming that all other gaseous species have the same velocities (Weng et al., 2018; Bongers and De Goey, 2003; Channel Flow, 2003)

$$D_{i,m} = \frac{1 - x_i}{\sum_{k \neq i} \frac{x_k}{D_{i,k}}} \tag{5}$$

where $D_{i,k}$ is the binary diffusivities for the species pairs present; x_k denotes the molar fraction of the gaseous species, k.

Considering the porosity of the GDL and CL, $D_{i,m}$ is corrected by the Bruggeman equation (Weng et al., 2018).

$$D_{i,m}^{eff} = \frac{1 - x_i}{\sum_{k \neq i} \frac{x_k}{\left(\varepsilon_{m,g}^{eff}\right)^{1.5} D_{i,k}}} \tag{6}$$

where $\varepsilon_{m,g}^{eff}$ is the effective porosity for gas, which is calculated in detail in the SI. The $D_{i,m}$ used in this work can be found in Table S3 in the SI.

The gas velocity, u_g, is obtained by the conservation equations of momentum and mass. The flow of gas mixture through the GASC is assumed to be laminar and compressible (Ma < 0.3) (Wu et al., 2015). The momentum balance can be described by Navier-Stokes equation as follow.

$$\rho_g (u_g \cdot \nabla) u_g = \nabla \cdot \left[-PI + \mu_g (\nabla u_g + (\nabla u_g)^T) - \frac{2}{3} \mu_g (\nabla \cdot u_g) I \right] + \rho_g g \tag{7}$$

where P is the total gas pressure, μ_g is the dynamic viscosity of the gas mixture, I is the identity tensor, and g is the gravitational acceleration.

In the GDL and CL, Darcy's law is selected to describe momentum balance of the laminar flow in the porous media (Serincan et al., 2009), thus

$$u_g = -\frac{k_{m,g}^{eff}}{\mu_g} \nabla P \tag{8}$$

where $k_{m,g}^{eff}$ is the effective permeability for gas in the porous medium. The details of $k_{m,g}^{eff}$ calculation is shown in the SI.

Applying the continuity equation for incompressible flow on gas species, the overall mass balance can be modelled by

$$\nabla \cdot (\rho_g u_g) = Q_m \tag{9}$$

where Q_m is the source term, which is zero in the GASC and the GDL. In the CL, it is the sum of gaseous reaction rates (see Table S1 in the SI).

2.1.3. Transport of aqueous species

The mass conservation of aqueous species, j, is modelled by Nernst−Plank equation (Zhang et al., 2014)

$$\nabla \cdot \left(-\rho_l D_{j,m} \nabla \omega_j - \frac{z_j F \rho_l \omega_j D_{j,m} \nabla V_l}{R_g T} + \rho_l \omega_j u_l \right) = R_{j,m} \tag{10}$$

where ρ_l is the density of the liquid mixture, z_j is the valence of the ionic species, V_l is the voltage of the electrolyte phase, R_g is the ideal gas constant, T is the operating temperature; u_l is the liquid velocity, which is the ratio of volumetric flowrate to cross-section area of the ELEC, and $D_{j,m}$ is the diffusivity of the aqueous species through porous media, which is also corrected by the Bruggeman equation.

2.1.4. Homogeneous reactions

In this work, we assume that the pH remains constant in the liquid phase, equivalent to the initial value of the inlet solution, owing to the continuous supply of electrolyte. Only homogeneous reactions under the alkaline condition are considered.

$$CO_{2(aq)} + OH^- \overset{k_{Ha}}{\rightarrow} HCO_3^- \tag{11}$$

$$HCO_3^- + OH^- \overset{k_{Hb}}{\rightarrow} H_2O + CO_3^{2-} \tag{12}$$

The reaction rates for $CO_{2(aq)}$, HCO_3^-, and $CO_3^{2-}$are expressed as

$$R_{H,CO_2(aq)} = -M_{CO_2} R_{Ha}; \quad R_{H,HCO_3} = -M_{HCO_3}(R_{Ha} - R_{Hb}); \\ R_{H,CO_3(aq)} = M_{CO_3} R_{Hb} \tag{13}$$

where M_{CO_2}, $M_{HCO_3}$and $M_{CO_3}$are molecular weights for CO_2, HCO_3^-, and CO_3^{2-}, respectively. R_{Ha} and R_{Hb} are the reaction rates for Eq. (11) and Eq. (12), and the calculation details can be found in the SI.

2.1.5. Gas-liquid mass transfer

In the CL, we only consider the gas-liquid mass transfer of CO_2 by neglecting the solubility of CO and H_2 (Weng et al., 2019a). Water condensation/evaporation is also ignored at given operating temperature, i.e., 60 °C (Xiang et al., 2019). The CO_2 gas-liquid mass transfer rate can by calculated by

$$R_{P,CO_2(aq)} = -R_{P,CO_2(g)} = a_{gl} K_{GL} M_{CO_2} \left(\frac{P_{CO_2(g)}}{H_{CO_2}} - C_{CO_2(aq)} \right) \tag{14}$$

where a_{gl} is the gas-liquid interfacial area, K_{GL} is the overall mass transfer coefficient, H_{CO_2} is Henry's constant for CO_2 dissolution in the electrolyte, which is calculated taking into account the salting-out effect, $P_{CO_2(g)}$ is the partial pressure of $CO_{2(g)}$, which is calculated according to Dalton's law, and $C_{CO_2(aq)}$ is the concentration of dissolved CO_2 in the electrolyte. More details about the calculation of a_{gl} and$H_{CO_2}$are given in the SI.

2.1.6. Electrode kinetics

The current densities of the reactions (1), (2) and (3), i_{Ea}, i_{Eb}, and i_{Ec}, are calculated by the Tafel kinetics (Weber and Newman, 2004)

$$i_{Ea} = -i_{o,Ea}^{ref} \left(\frac{C_{CO_2(aq)}}{C_{CO_2(aq),Ea}^{ref}} \right) \exp \left(-\frac{\beta_{Ea} F}{R_{ideal} T} (V_s - V_l - V_{eq,Ea}^{ref}) \right) \tag{15}$$

$$i_{Eb} = -i_{o,Eb}^{ref} \left(\frac{C_{CO_2(aq)}}{C_{CO_2(aq),Eb}^{ref}} \right) \exp \left(-\frac{\beta_{Ea} F}{R_{ideal} T} (V_s - V_l - V_{eq,Eb}^{ref}) \right) \tag{16}$$

$$i_{Ec} = -i_{o,Ec}^{ref} \exp \left(-\frac{\beta_{Ec} F}{R_{ideal} T} (V_s - V_l - V_{eq,Ec}^{ref}) \right) \tag{17}$$

where $i_{o,Ea}^{ref}$, $i_{o,Eb}^{ref}$ and $i_{o,Ec}^{ref}$ are the exchange current densities per catalyst surface area at the reference condition corresponding to reactions (1) to (3), $C_{CO_2(aq),Ea}^{ref}$, $C_{CO_2(aq),Eb}^{ref}$are the reference concentrations of $CO_{2(aq)}$ corresponding to reactions (1) and (2); β_{Ea}, β_{Eb}, and β_{Ec} denote the symmetry factor corresponding to the formation of $HCOO^-$, CO, and H_2, F is the Faraday constant, $V_{eq,Ea}^{ref}$, $V_{eq,Eb}^{ref}$ and $V_{eq,Ec}^{ref}$ are the equilibrium potentials for reactions (1) - (3) at the reference condition and operating temperature, respectively. The local electronic and electrolyte potential, V_s and V_l are derived by Ohm's law coupled with charge conservation (Wu et al., 2015). The specific calculation process can be found in the SI.

The electrochemical reaction rates for $CO_{2(aq)}$, $HCOO^-$, CO and H_2 are expressed according to Faraday's law:

$$R_{E,CO_2(aq)} = \frac{M_{CO_2} a_{sl}(i_{Ea} + i_{Eb})}{2F}; \quad R_{E,HCOO} = -\frac{M_{HCOO} a_{sl} i_{Ea}}{2F}; \\ R_{E,CO} = -\frac{M_{CO} a_{sl} i_{Eb}}{2F}; \quad R_{E,H_2} = -\frac{M_{H_2} a_{sl} i_{Ec}}{2F} \tag{18}$$

where M_{HCOO}, M_{CO}, and M_{H2} are molecular weights for $HCOO^-$, CO, and H_2, respectively. a_{sl} is the specific solid-liquid interfacial area which can be seen in the SI.

2.1.7. Boundary conditions

The gaseous species are modelled collectively in the GASC, GDL and CCL. In this work, we assume that CO_2 can penetrate through the membrane and reduced to formic acid inside the ACL, in addition to the reduction to CO inside the CCL. Zero flux of gaseous species is set at the ELEC/ACL interface. At the inlet of the GASC, the mixture gas composition and velocity are set to the initial values of the feed-in mixture gas (Wu et al., 2015). At the outlet of the GASC, the outlet mixture gas is at ambient pressure of 1 atm. The aqueous species are mainly modelled in the ACL and ELEC, with the initial feed-in electrolyte concentration at the ELEC inlet and zero flux at the GASC/GDL interface. The porous media, i.e., GDL and CCL are assumed to be partially filled with electrolyte with a pre-defined saturation level. Open boundaries are set for the concentrations of gaseous and aqueous species at the GASC and ELEC outlets, respectively. A constant applied cathode potential, $V_{c,RHE}$, is applied on the GASC/GDL interface. The anode potential, $V_{a,\ RHE}$, is calculate separately by considering various losses (Baker, 1993; Buck, 1984; Björnbom, 1986). The difference of $V_{c,RHE}$ and $V_{a,RHE}$ is the practical applied cell voltage, that is used for calculating the electrical energy consumption.

2.1.8. Model-Based performance evaluation

The single-pass product yield (PY), CO_2 conversion (CR) and specific electrical energy consumption (SEEC) are chosen as the three performance indicators of the GDE-based microfluidic electrochemical CO_2 reduction process.

PY (kg s^{-1}), defined as mass of mixed product (CO and formate), is calculated by the following expressions:

$$PY_{HCOO} = -\frac{a_{sl} M_{HCOO} W_{ele} \int_0^{H_{ele}} \int_0^{L_{CL}} i_{Ea} dx dy}{2F}; \\ PY_{CO} = -\frac{a_{gl} M_{CO} W_{ele} \int_0^{H_{ele}} \int_0^{L_{CL}} i_{Eb} dx dy}{2F} \tag{19}$$

$$PY = PY_{HCOO} + PY_{CO} \tag{20}$$

where W_{ele} and H_{ele} are the width and height of the ELEC, L_{CL} is the length of the CL. The detailed values can be found in Table S1 of the SI.

CR (%), defined as the mole ratio of product to feed CO_2, indicating the ratio of CO and formate with respect to the reactant CO_2, is calculated by:

$$CR = \frac{n_{CO} + n_{HCOO}}{n_{CO_2}} \times 100\% \tag{21}$$

in which the amount of CO, formate and CO_2 are calculated by the following expressions, respectively.

$$n_{CO} = \frac{PY_{CO}}{M_{CO}}; \quad n_{HCOO} = \frac{PY_{HCOO}}{M_{HCOO}}; \quad n_{CO_2} = \frac{u_G A_{GASC} y_{CO_2(g)}^{in}}{0.0224(m^3 mol^{-1})} \tag{22}$$

where A_{GASC} is cross-sectional area of the GASC, which can be found in the SI, $y_{CO_2(g)}^{in}$ is the mole fraction of CO_2 at the gas inlet (see Table 1).

Table 1
Ranges of design variables of the electrolyser.

Design variable	Symbol(unit)	Range
Cathode potential	$V_{c,RHE}$ (V)	$-1 \sim -0.2$
Feed gas velocity	u_G (m s^{-1})	$5 \times 10^{-3} \sim 2 \times 10^{-2}$
Electrolyte flow velocity	u_L (m s^{-1})	$1 \times 10^{-5} \sim 5 \times 10^{-5}$
Mole fraction of CO_2	$y_{CO_2(g)}^{in}$ (%)	$50 \sim 100$
Electrolyte concentration	c_{OH}^{in} (M)	$0.01 \sim 0.5$
Electrolyte channel width	H_{ele} (m)	$0.02 \sim 0.08$
Intrinsic porosity of GDL	ε_{GDL}	$0.2 \sim 0.8$
Catalyst loading	m_{cat} (kg m^{-2})	$0.01 \sim 0.05$

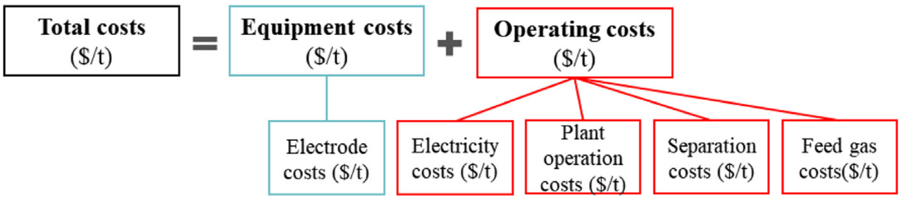

Fig. 2. Definition of the costs covered within the techno-economic assessment.

SEEC (kWh kg^{-1}), defined as the electric energy consumption for producing unit mass of the mixed product, is calculated by

$$SEEC = \frac{FV_{app}}{M_{HCOO}FE_{HCOO}} + \frac{FV_{app}}{M_{CO}FE_{CO}} \tag{23}$$

where V_{app} represents the applied cell voltage, which is the difference between the anode and cathode voltages, FE_{HCOO} and FE_{CO} are the Faraday efficiencies of formate and CO production, which are the important indicators representing the electrochemical selectivity. The detailed calculations can be found in the SI.

2.1.9. Techno-economic analysis

In this work, the techno-economic analysis (TEA) mainly concentrates on a total plant-gate levelised cost of production in units of $ per tonne (1000 kg) of products, including CO and formate. Fig. 2 shows the definition of the costs covered within the TEA. The costs are broadly divided into two categories, including equipment and operating costs, respectively. The equipment cost only refers to the cost of the electrodes without considering the cost of other infrastructure. The operating cost includes electricity, plant operation, product separation and feed gas costs. Concentrated CO_2 with market price is used as the reactant. Renewable or clean energy (photovoltaic power) is selected as the electricity source. The specific calculation equations, parameters and assumptions involved can be seen in the SI. The lifetime of the plant is assumed to be 30 years, which is the average lifetime of current chemical plants (Palmer et al., 2018).

2.2. Data-driven machine learning surrogate models

A hybrid data-driven machine learning algorithm, extended adaptive hybrid functions (E-AHF), is selected to conduct the multi-variable and multi-objective optimisation of the GDE-based electrochemical CO_2 reduction process. The E-AHF algorithm can fully use five different individual surrogate models by automatically placing weight factors in a pointwise way. The implemented surrogate models include support vector regression (SVR), Kriging (KRG), polynomial response surface (PRS), radial basis function (RBF) and moving least squares (MLS). Fig. 3 briefly shows the calculation process of the E-AHF surrogate model.

In part 1, there are three steps for the generation of datasets (by the physics-based model) used for training and testing the surrogate model. Firstly, a design of experiments (DoE) method, namely Latin hypercube sampling (OLHS), is selected for obtaining different datapoints, which are used as the initial values of the input variables of the multi-physics model to calculate the corresponding output values. Part 2 is the selection of individual model with the best prediction performance, characterised by the normalised error (EN_i) (detailed expressions can be seen in the SI). A threshold value β within the range of [0,1] is defined for selection of the individual surrogate models. When the value of EN_i is smaller than β, the corresponding individual surrogate model is selected as a candidate surrogate model for the next part. Part 3 is to calculate the adaptive weight factors (ω) for the hybrid model consisting of the surrogate models selected in part 2. The three steps in this part are local measure estimation, probability estimation, and local weight determination. More specific details and expressions about part 3 can be found in the SI. After this process, the weight factors of different individual surrogate models and the weighted combination for all datapoints are determined for the lowest prediction error.

The predicted response ($\hat{y}$) by the E-AHF model can be calculated by the following equation.

$$\hat{y}(x) = \sum_{i=1}^{m} \omega_i(x)\hat{y}_i(x) \tag{24}$$

where $\hat{y}(x)$ is the predicted response by the hybrid model at the input vector x, $\hat{y}_i(x)$ is the predicted response by the ith individual surrogate model at the input vector x; m is the number of surrogate models in the hybrid surrogate; $\omega_i(x)$ is the weight factor of the ith individual surrogate model at point x.

Three E-AHF models are developed for predicting the single-pass product yield (PY), conversion ratio (CR) and specific electrical energy consumption (SEEC), respectively.

2.3. Sobol's global sensitivity analysis

In contrast to local sensitivity, global sensitivity assesses the overall impact of a specific design variable on a system. Consequently, global sensitivity analysis (GSA) serves to enhance our comprehension of the relationships between design variables and objectives, as well as to categorise the influence of each individual variable. This, in turn, aids researchers in concentrating their efforts on the design variables that exert a more significant influence. Sobol's GSA, a variance-based Monte Carlo method, enables the calculation of sensitivity indices for individual parameters and the evaluation of interactions amongst these parameters by examining the ratio of each sensitivity index to the corresponding total sensitivity index. An in-depth explanation of the expressions utilised in Sobol's GSA could be found elsewhere (Xing et al., 2013).

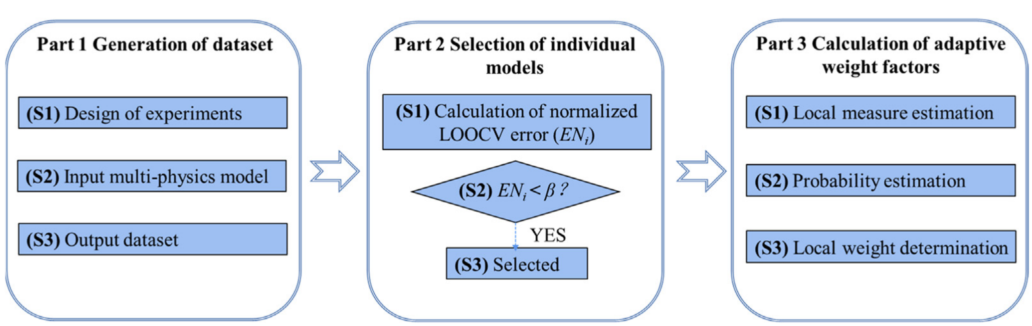

Fig. 3. Calculation flow chart of E-AHF surrogate model.

2.4. Multi-variable and multi-objective optimisation

After successfully creating a reliable E-AHF surrogate model that accurately capture the relationships between multiple design variables and objective functions, a non-dominated sorting genetic algorithm II (NSGA-II) (Deb et al., 2002; Sumida et al., 1990), an updating version of genetic algorithm (GA), was adopted to search for the Pareto front of multiple objective functions and conduct the multi-objective optimisation. NSGA-II is a posteriori approach, which is used for multi-objective optimisation problems, where the goal is to find a set of solutions that optimise multiple conflicting objectives simultaneously. NSGA-II does not require prior knowledge of the Pareto front (the set of optimal solutions), and it iteratively evolves a population of candidate solutions to discover a diverse set of non-dominated (Pareto-optimal) solutions. The suitability for parallel computation and for larger solution spaces makes NSGA-II more suitable for multi-objective optimisation than other optimisation algorithms (simulated annealing and Bayesian optimisation) (Zhao et al., 2016; Putra et al., 2019).

The objective of the multi-optimisation is to identify the optimal trade-off solutions of PY, CR and SEEC, which strike a balance between the three objectives by maximising PY and CR while minimising SEEC. Eight design variables are optimised, including three electrode parameters and five operational conditions. The ranges of these eight design variables are shown in Table 1.

2.5. Numerical solution method

Commercial software COMSOL Multiphysics 5.6 is used to solve the fully coupled governing equations of the multi-physics models based on the finite element method (FEM). The spatial distribution of dependant variables over the 2D geometry are obtained through solution of the corresponding partial differential equations (PDEs) using the built-in modules. The MUMPS stationary solver is chosen with default parameter settings and computational tolerance was set to be physics-controlled with a relative tolerance of 0.01. An online tool DADOS (http://app.dados.com.cn) is applied to perform the E-AHF surrogate modelling. The multi-variable and multi-objective optimisation are implemented by NSGA- II in Matlab. A laptop equipped with Intel® i9 processor @2.40 GHz and 64 GB RAM is used for modelling and simulation. The required computational time to solve the physics-based model is about 5 min each case, depending on the values of design variables. On contrary, it only requires less than 1 min to train the E-AHF model using 100 data samples and obtain the optimal design variables and objective functions when NSGA-II is implemented.

3. Results and discussion

3.1. Validation of the physics-based model

The cathode GDE utilised in this study was fabricated by applying a solution of Cu_xO catalyst ink (Sigma-Aldrich) and Nafion® ionomer (5%, DuPont) onto a hydrophobic carbon paper (H2315 I2, Freudenberg). The process for preparing the Cu_xO electrode catalyst ink was as follows: 15 mg of Cu_xO nanoparticles and 33 μL of Nafion were mixed in 200 mL of isopropanol, and this mixture was subjected to ultrasonic dispersion for 60 min to achieve a homogeneous solution. The amount of catalyst applied was meticulously controlled by weighing it both before the ink was sprayed and after it had dried in the oven to ensure it met the requirement of 1 mg cm^{-2}. The electrolyser consists of a 1 × 1 cm^2 cathode GDE and a nickel foam anode, which served as both a gas diffusion layer and a catalyst for the oxygen evolution reaction. An anion exchange membrane (AEM) was used, along with serpentine-shaped cathode and anode flow plates to facilitate the delivery of reactants. Titanium flow field plates were machined with serpentine channels measuring 1 mm in width and 1 mm in depth, with a channel length of 10 mm.

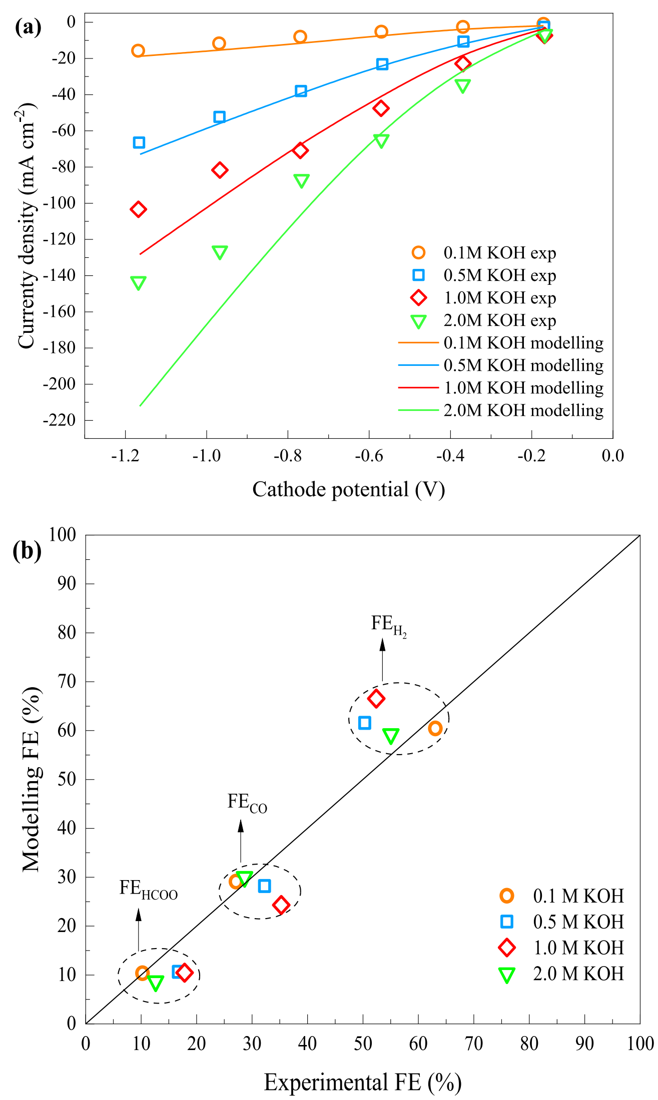

Fig. 4. Experiment validation of the physics-based model for the GDE-based microfluidic eCO_2RR process: (a) current density, (b) Faraday efficiency.

These flow plates were positioned around the Membrane Electrode Assembly (MEA) and played a role in directing reactants and products to and from the reaction interface. The MEAs themselves consisted of a silver-coated cathode GDE, an AEM and nickel foam anode measuring 1 × 1, 3 × 3 and 2 × 2 cm^2, respectively. The cathode GDE was positioned within a square window of the same area on the gasket, which was securely attached to the bipolar plates and the grooved flow field.

The cathode received a supply of humidified CO_2 gas at a rate of 100 standard cubic centimeters per minute (SCCM) through a flow control system consisting of a flow controller (Sevenstar D07–19) and a water bath. In contrast, the anode was supplied with recirculated 1 M KOH at a flow rate of 20 ml per minute. All electrochemical experiments were conducted using an electrochemical workstation (PMC−CHS08A). The potentiostatic test involved applying current densities up to 200 mA cm^{-2}. The performance characterisation of CO_2 electrolysis was carried out after achieving stable operation for 25 min at standard temperature and pressure. Gas chromatography (Agilent 8890) was used to measure the mole fraction of the products present in the gaseous output.

The reliability and accuracy of the physics-based mechanistic model are validated by experimental data before the mechanistic model is used to generate data for surrogate model training. As shown in Fig. 4, the effect of cathodic potential, with respect to different electrolyte concentrations, on current density and Faraday efficiency (FE) of different products, i.e., CO, HCOO and H_2, are presented. More details of the experiment could be found elsewhere (Yang et al., 2021b). The results indicate that the mechanistic model yields precise predictions at low potential magnitudes, i.e., 0.6 V, and low electrolyte concentrations, i.e., 0.0.5 M. However, above 0.5 M and 0.6 V, the disparity between the experimental data and the modelling results gradually amplifies as the electrolyte concentration and cathode potential magnitude increase, owing to the elevated electrochemical reaction and the associated more complex mass transport. Therefore, in our work, the range of electrolyte concentration is set to 0.01–0.5 M (Table 1), within which the model exhibits an acceptable degree of prediction accuracy and reliability.

3.2. Evaluation and analysis of E-AHF models

After the mechanistic model validation, 100 data points generated by OLHS are used to evaluate the E-AHF models, in which 80% and 20% of the data (see Table S4 in the SI) are used for surrogate model training and testing, respectively. As shown in Table 2, the calculated R^2 for all three objective functions, i.e., PY, CR and SEEC, are higher than 0.96, indicating the good prediction accuracy of the E-AHF surrogate models. In this context, 100 data samples were selected since adding more data samples beyond this point only results in marginal improvement in prediction accuracy (see Table S6 in the SI). Fig. 5 shows the correlations of the actual (mechanistic model output) and predicted (E-AHF surrogate model output) values for the three objective functions (PY, CR and SEEC), demonstrating the good consistency for all three objectives. The relative errors of all three objective functions (Fig. 5d) are below 15% and 95% of the relative errors are in the range 0 – 5% for the predictions of PY and SEEC. These results indicate that the E-AHF model is a satisfactory surrogate model for the prediction of PY, CR and SEEC for the GDE-based eCO_2RR process within the study ranges.

Table 2
Key parameters setting and calculated R^2 of E-AHF models.

Objective functions	Threshold value (β)	R-squared (R^2)
PY	0.5	0.9640
CR	0.5	0.9862
SEEC	0.5	0.9781

3.3. Sensitivity analysis of E-AHF models

Prior to multi-variable and multi-objective optimisation, sensitivity analysis is conducted to understand the significance of different design variables on objective functions. Fig. 6 shows the results of the Sobol global (S^T) sensitivity analysis of the eight design variables with respect to the three objective functions, i.e., PY, CR and SEEC. It can be identified from the figure that the electrolyte concentration (c_{OH}^{in}) is the design variable with the most significant influence on PY and CR, and its effect on SEEC is only less significant than that of the cath-

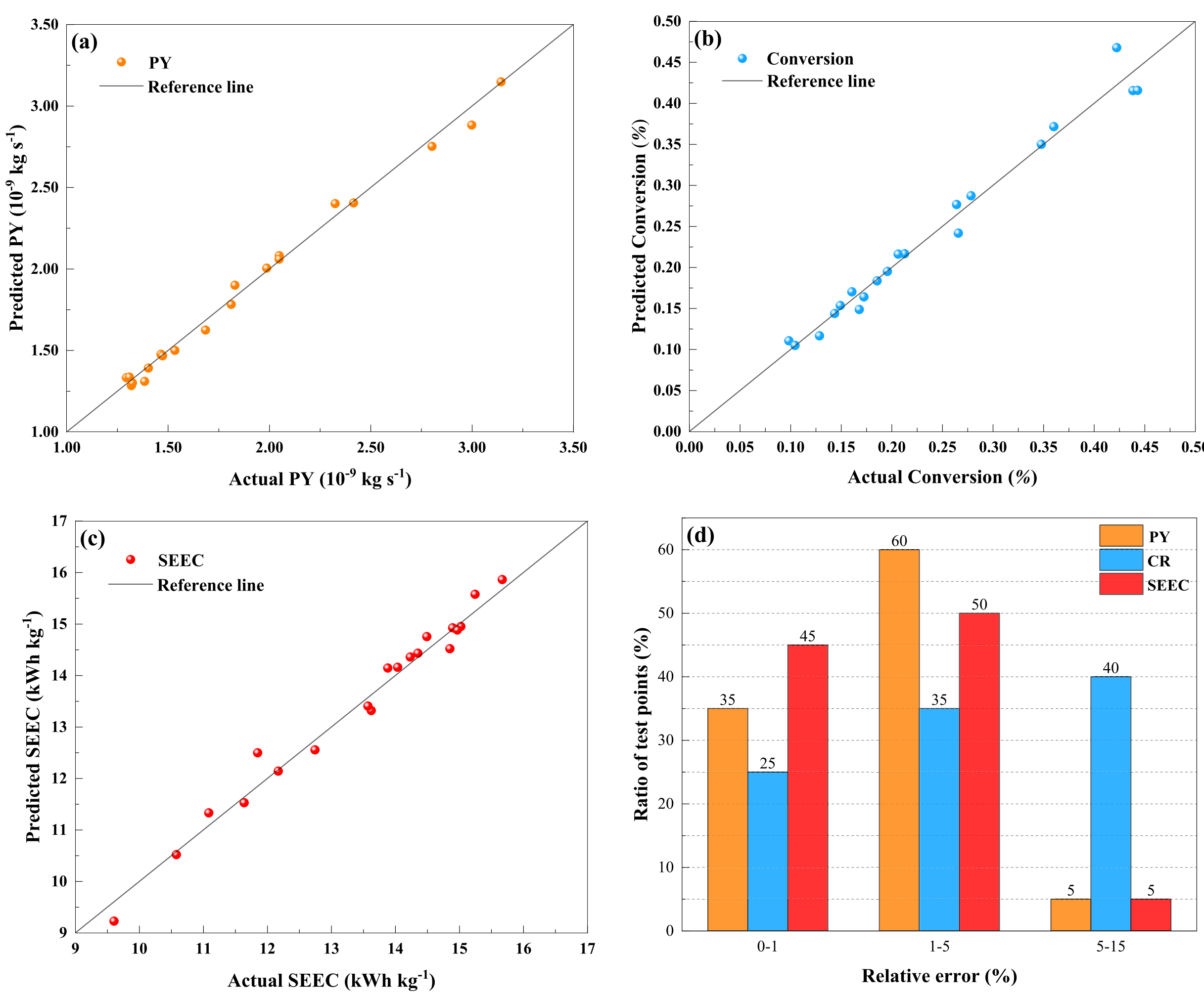

Fig. 5. E-AHF model analysis: actual and predicted values correlation of (a) product yield (PY), (b) conversion ratio (CR) and (c) specific electrical energy consumption (SEEC); (d) relative error distribution of PY, CR and SEEC prediction.

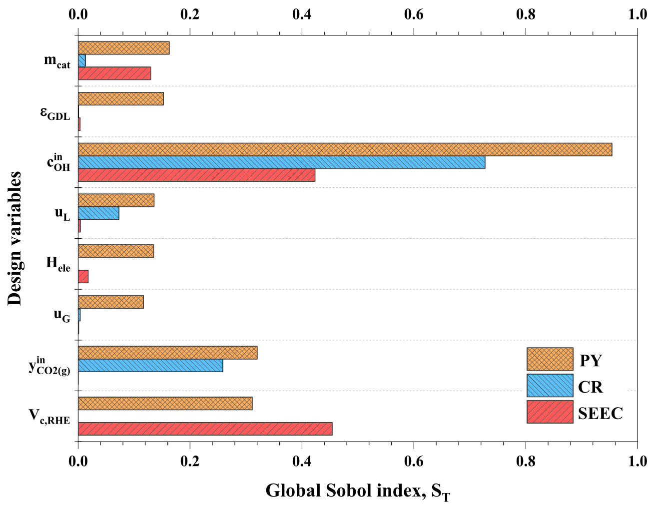

Fig. 6. Sobol global sensitivity analysis of design variables in E-AHF model of GDE process. The lengths of columns demonstrate the global sensitivity index and the orange, blue and red columns represent PY, CR and SEEC, respectively.

ode potential $V_{c,RHE}$, which has the greatest impact on SEEC. The relatively long orange column of $V_{c,RHE}$ also shows the remarkable influence of cathode potential on PY. Apart from the variables that significantly affect at least two objective functions, some variables have noticeable influence on only one objective, e.g., u_G and ε_{GDL} influence only PY to any great extent with a relatively low sensitivity for CR and SEEC.

3.4. Multi-variable and multi-objective optimisation

The three objective functions, i.e., PY, CR and SEEC, are interdependent and affect each other in practical operation. The purpose of multi-objective optimisation for this process is to identify the trade-off solutions that strike a balance between PY, CR and SEEC. The optimal solutions prioritise larger PY and CR while simultaneously aiming for smaller SEEC. For this purpose, NSGA-II is chosen to implement the triple-objective optimisation, in which the key parameters include the population size, number of generations, crossover distribution index, mutation distribution index, tournament size (Table S5 in the SI). Fig. 7 shows the optimal Pareto set obtained from the optimisation over the data points. Depending on the various requirements of PY, CR and SEEC, we can choose different points as the final optimal trade-off solutions. The green symbol point in Fig. 7 is the optimal trade-off solution which is identified using equal weights (i.e., 1/3) for the three objectives of PY, CR and SEEC. The curves in Fig. 7(b)–(d) are the trade-off solutions of dual parameters, i.e., PY-CR, PY-SEEC and CR-SEEC, respectively. The upper limit of the ranges of the design variables in Table 1 are chosen as the base case condition. The values of design variables in base case and optimal conditions, as well as the corresponding obtained objectives are listed in Table 3.

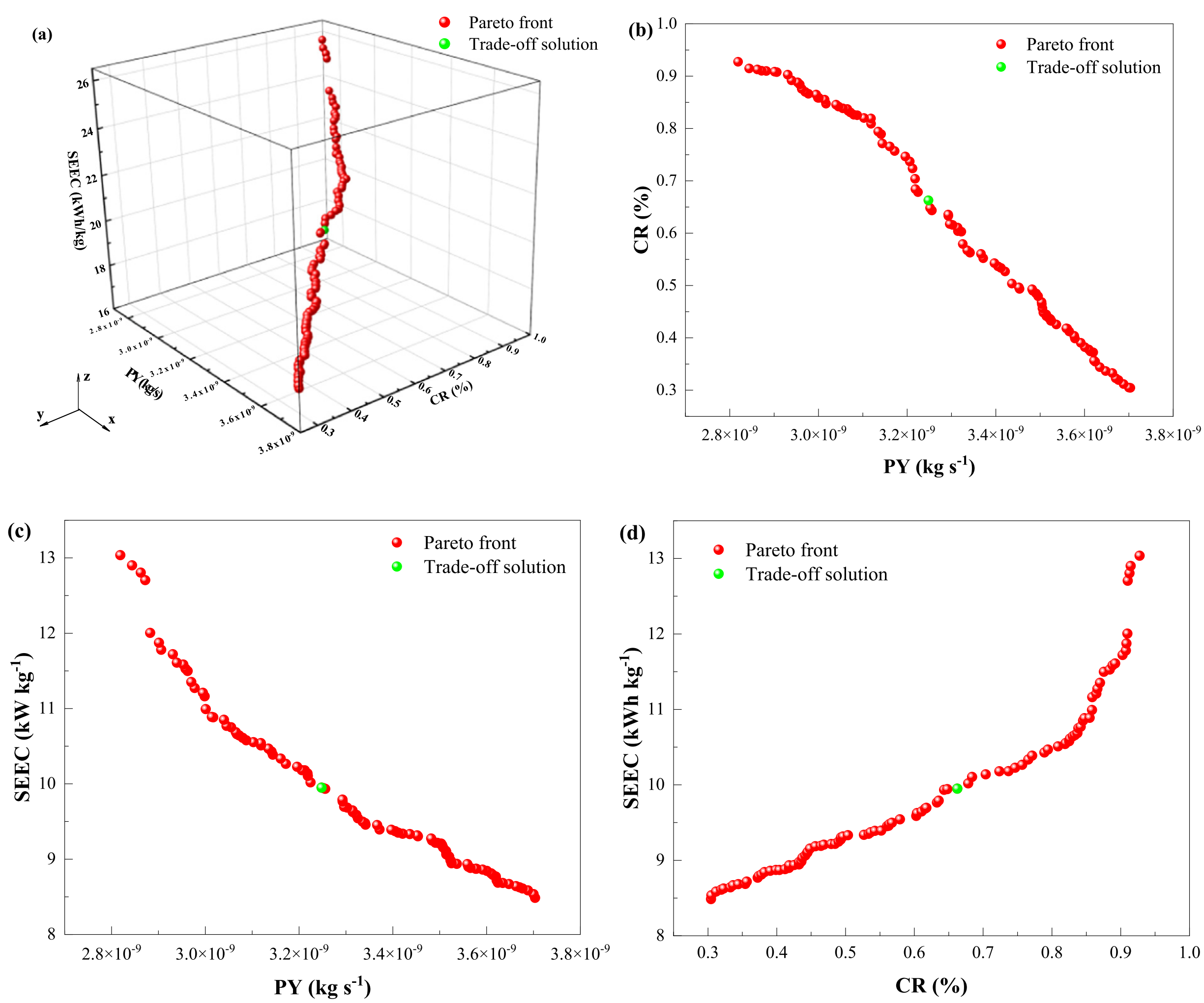

Fig. 7. Results for the multi-objective optimisation of the GDE-based eCO_2RR electrolyser by NSGA-II.

Table 3
Multi-optimisation results and the corresponding optimal design variables.

Parameter	Base case	Trade-off case
Cathode potential $V_{c,RHE}$ (V)	−0.20	−0.24
Feed gas velocity u_g (m s^{-1})	2×10^{-2}	9.3×10^{-3}
Electrolyte flow velocity u_l (m s^{-1})	5.00×10^{-5}	4.55×10^{-5}
Mole fraction of inlet CO_2 $y^{in}_{CO_2(g)}$ (%)	100	50.01
Electrolyte concentration c^{in}_{OH} (M)	0.5	0.01
Electrolyte channel width H_{ele} (m)	0.08	0.0698
Intrinsic porosity of GDL ε_{GDL}	0.80	0.56
Catalyst loading m_{cat} (kg m^{-2})	0.05	0.013
PY (kg s^{-1})	1.36×10^{-9}	3.25×10^{-9}
CR (%)	0.0693	0.6626
SEEC (kWh kg^{-1})	15.6299	9.9498

It can be seen in Fig. 7 that both CR and SEEC decreases as PY increases, implying that CR and SEEC exhibits similar changing trends in all optimal sets. The improved CR leads to an increase in SEEC, indicating that the higher conversion is at the cost of higher energy consumption. The specific value of final optimal trade-off case can be seen in Table 3, in which the single-pass PY, CR and SEEC are 3.25×10^{-9} kg s^{-1}, 0.6626% and 9.9498 kWh kg^{-1}, respectively. After the multi-optimisation process, notable improvements are observed in three objective functions of the GDE-based microfluidic eCO_2RR process, as compared to the results before optimisation. Specifically, the SEEC value is reduced by nearly 50%, from 15.63 to 9.95 kWh kg^{-1}. Additionally, the value of PY and CR are more than doubled compared to the base case before optimisation.

By analysing the design variables of the trade-off case, the larger cathode potential ($V_{c,RHE}$) and electrolyte flow velocity (u_l) tend to result in better optimal results. In the trade-off case, the values of $V_{c,RHE}$ and u_l are −0.24 V and 4.55×10^{-5} m s^{-1}, respectively, which are both near to the largest value of in the study range. But it is worth noting that too large $V_{c,RHE}$ may impact the wetting characteristics of the hydrophobic GDL, which will eventually limit the performance of the GDE-based eCO_2RR electrolyser. The results are consistent with the work of Yang et al. (2021a). In contrast, the values of mole fraction of CO_2 ($y^{in}_{CO_2(g)}$) and electrolyte concentration (c^{in}_{OH}) are 50% and 0.01 M, which are both very close to the lower boundaries of study range, indicating that the small value of $y^{in}_{CO_2(g)}$ and c^{in}_{OH} may be beneficial. Although higher $y^{in}_{CO_2(g)}$ improves the rate of reactions (1) and (2), but the effect is relatively small in our study range (50%–100%). CO_2 will not be fully used if its concentration at the inlet is too high, which will reduce the CR of CO_2 and increase the SEEC, e.g., the trade-off CR is ten times lower than that in the base case. Moreover, CO2 could directly react with OH- in addition to the electrochemical reactions (1) and (2). At high KOH concentrations, the CO_2 buffering reaction is accelerated by concentrated OH-, that lowers the chances of CO_2 participating in electrochemical conversion reactions, leading to the drop of CR. There is the other reason beyond the mechanistic model in our work, that is the notable C_2 products (i.e., ethyl alcohol and ethylene) generated at higher c^{in}_{OH} (Xiang et al., 2019), although the C_2 products are not included in the model. This process will consume the feed CO_2 gas and further affect the PY and CR values. Moreover, the higher concentration of OH^-reduces the rate of reactions (1) and (2).

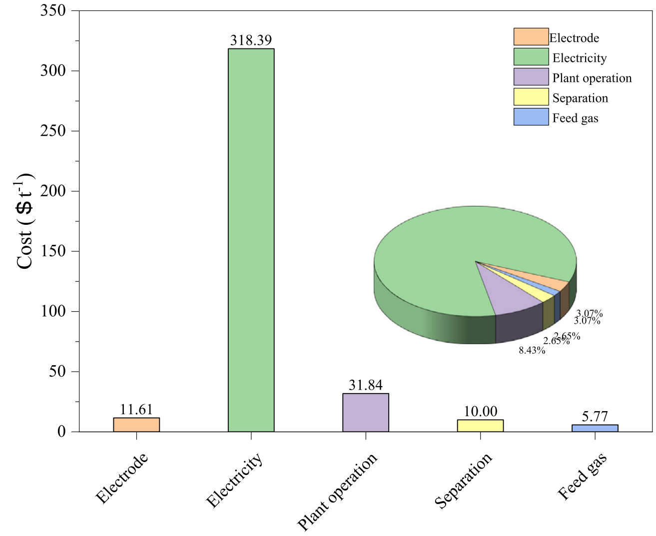

Fig. 8. Composition of total costs in GDE-based electrochemical CO_2 reduction process.

3.4. Techno-economics of the GDE-based eCO_2RR process

Some cost-related assumptions are made according to De Luna et al. (2019), e.g., the price of pure CO_2 is assumed as $30 per ton. More details of the costs calculation could be found in the SI. Table 4 shows the production cost and CO_2 emissions of the GDE-based eCO_2RR process based on the trade-off solution obtained from multi-objective optimisation and the comparison with other chemical production technologies, e.g., CO_2 utilisation plant and fossil-based processes. The CO_2 emissions related to CO/formate production are very different from the various technologies; fossil fuel-derived technology would produce additional CO_2 but the eCO_2RR route is one of the negative emissions technologies (NET). The production cost for CO and formate for the eCO_2RR process is about 378 $ t^{-1} product, which is much lower than the cost of a CO_2 utilisation plant (835 $ t^{-1} product) but higher than that of conventional fossil fuel-derived technology at 315 $ t^{-1} product. However, conventional CO/formate production by fossil fuel-derived technology has substantial CO_2 emissions associated with the fossil fuel feedstocks (>1 tCO_2 t^{-1}product). Fig. 8 shows the composition of total costs for the GDE-based eCO_2RR process. The feed gas cost is lowest with the value of 5.77 $ t^{-1} because most feed gas can be recycled from the outlet gas. The dominant contribution to the overall cost is electricity (80%) with a value of 318.39 $ t^{-1}. Hence, a lower electricity price will generate a significant reduction in total production cost; such savings might be achievable with the further development of renewable or clean energy technologies. Thus, despite its higher costs of production, the GDE-based electrochemical carbon dioxide reduction associated with renewable or

Table 4
Comparison of production cost and carbon emissions across various technology processes.

Technology	Production cost ($ t^{-1} product)	CO_2 emissions (tCO_2 t^{-1}product)
Electrochemical	378	< 0
CO_2 utilisation plant* [34]	835	0–0.25
Fossil fuel-derived** [33]	315	> 1

* CO_2 utilisation plant: CO_2 transformation process into another product with commercial value.
** Fossil fuel-derived technologies: (i) conventional CO synthesis (ii) methyl formate hydrolysis.

clean energy supplies offers a negative emission route to the production of core pre-cursor chemicals, CO and formate.

4. Conclusions

A multi-variable and multi-objective optimisation of a GDE-based microfluidic electrochemical CO_2 reduction process was conducted. A two-dimensional multi-physics model was first developed and experimentally validated, which is then used to build a database to train the surrogate model based on the extended adaptive hybrid functions (E-AHF). The effects of eight design variable, including three electrode parameters and five operational conditions on three objective functions, i.e., the single-pass product yield (PY), CO_2 conversion (CR) and specific electrical energy consumption (SEEC) were studied. NSGA-II was implemented to search for the trade-off solutions of the maximum PY and CR and the minimum SEEC. The cost of the eCO_2RR process in the trade-off condition was also conducted. The main findings of this work is presented as follow:

1. E-AHF surrogate models demonstrated their accuracy in replacing the physics-based model for rapid prediction of the performance (PY, CR and SEEC). The R^2 for the three objective functions are all higher than 0.96, and the prediction relative errors are lower than 15% for CR and lower than 5% for PY and SEEC.
2. The electrolyte concentration is the most sensitive variable for PY and CR and the cathode potential has the most significant impact on SEEC.
3. After optimisation, the performance of the eCO_2RR system is significantly improved, e.g., the SEEC is reduced by nearly half and PY and CR are nearly doubled. The trade-off of the three objective functions is obtained, in which the corresponding optimal single-pass PY, CR and SEEC are 3.25×10^{-9} kg s^{-1}, 0.663% and 9.9498 kWh kg^{-1} based on flow channels with 1 cm in length, respectively. The corresponding optimal catalyst loading, GDL porosity, electrolyte channel width are 0.013 kg m^{-2}, 0.56 and 0.0698 m, respectively. The optimal cathode potential, reactant gas velocity, electrolyte velocity, inlet CO_2 mole fraction and electrolyte concentration are −0.24 V, 9.30×10^{-3} m s^{-1}, 4.55×10^{-5} m s^{-1}, 50.01% and 0.01 M, respectively.
4. The net production cost in the trade-off scenario is about 378 \$ t^{-1}, lower than a traditional CO_2 utilisation plant, with 80% of the cost attributed to electricity usage. Thus, a crucial factor in enhancing the economic efficiency of the GDE-based eCO_2RR process lies in acquiring cleaner and more affordable sources of renewable energy.

Declaration of Competing Interest

The authors declare that they have no known competing financial interests or personal relationships that could have appeared to influence the work reported in this paper.

Acknowledgement

The authors acknowledge the financial support of UK Engineering and Physical Sciences Research Council (EPSRC) under the grant numbers EP/W018969/2, EP/V042432/1 and EP/ V011863/1, and the Leverhulme Trust under grant number PLP-2022-001.

Supplementary materials

Supplementary material associated with this article can be found, in the online version, at doi:10.1016/j.ccst.2023.100138.

References

Baker, D.R., 1993. Reducing nonlinear systems of transport equations to Laplace's equation. SIAM J. Appl. Math. 53 (2), 419–439.
Björnbom, P., 1986. Influence of diffusion resistances on gas diffusion electrodes. J. Electrochem. Soc. 133 (9), 1874.
Blake, J.W., Padding, J.T., Haverkort, J.W., 2021. Analytical modelling of CO2 reduction in gas-diffusion electrode catalyst layers. Electrochim. Acta 393, 138987.
Bongers, H., De Goey, L.P.H., 2003. The effect of simplified transport modeling on the burning velocity of laminar premixed flames. Combust. Sci. Technol. 175 (10), 1915–1928.
Bouhlel, M.A., Martins, J.R.R.A., 2019. Gradient-enhanced kriging for high-dimensional problems. Eng. Comput. 35 (1), 157–173.
Buck, R.P., 1984. Kinetics of bulk and interfacial ionic motion: microscopic bases and limits for the nernst–Planck equation applied to membrane systems. J. Membr. Sci. 17 (1), 1–62.
Budzianowski, W.M., 2012. Value-added carbon management technologies for low CO2 intensive carbon-based energy vectors. Energy 41 (1), 280–297.
Channel Flow. In Chemically Reacting Flow, 2003; pp 309–334.
Deb, K., Pratap, A., Agarwal, S., Meyarivan, T., 2002. A fast and elitist multiobjective genetic algorithm: NSGA-II. IEEE Trans. Evol. Comput. 6 (2), 182–197.
De Luna, P., Hahn, C., Higgins, D., Jaffer, S.A., Jaramillo, T.F., Sargent, E.H., 2019. What would it take for renewably powered electrosynthesis to displace petrochemical processes? Science 364 (6438), eaav3506.
De Mot, B., Hereijgers, J., Duarte, M., Breugelmans, T., 2019. Influence of flow and pressure distribution inside a gas diffusion electrode on the performance of a flow-by CO2 electrolyzer. Chem. Eng. J. 378, 122224.
Durkin, A.; Guo, M., Surrogate-based optimisation of process systems to recover resources from wastewater (preprint). 2023 10.48550/arXiv.2305.05743.
Gabardo, C.M., O'Brien, C.P., Edwards, J.P., McCallum, C., Xu, Y., Dinh, C.T., Li, J., Sargent, E.H., Sinton, D., 2019. Continuous carbon dioxide electroreduction to concentrated multi-carbon products using a membrane electrode assembly. Joule 3 (11), 2777–2791.
García de Arquer, F.P., Dinh, C.T., Ozden, A., Wicks, J., McCallum, C., Kirmani, A.R., Nam, D.H., Gabardo, C., Seifitokaldani, A., Wang, X., Li, Y.C., Li, F., Edwards, J., Richter, L.J., Thorpe, S.J., Sinton, D., Sargent, E.H., 2020. CO2 electrolysis to multicarbon products at activities greater than 1 A cm^{-2}. Science 367 (6478), 661–666.
Higuchi, E.; Ueda, Y.; Chiku, M.; Inoue, H.J.E., Electrochemical hydrogenation reaction of toluene with PtxRu alloy catalyst-loaded gas diffusion electrodes. 2018, 9, 226–235.
Hori, Y., Wakebe, H., Tsukamoto, T., Koga, O., 1994. Electrocatalytic process of CO selectivity in electrochemical reduction of CO2 at metal electrodes in aqueous media. Electrochim. Acta 39 (11), 1833–1839.
Hossain, N., Mahlia, T.M.I., Zaini, J., Saidur, R., 2019. Techno-economics and sensitivity analysis of microalgae as commercial feedstock for bioethanol production. Environ. Prog. Sustain. Energy 38 (5), 13157.
Jiang, H., Wang, S., Xing, L., Pinfield, V.J., Xuan, J., 2023. Machine learning based techno-economic process optimisation for CO2 capture via enhanced weathering. Energy AI 12, 100234.
Kwok, K.S., Wang, Y., Cao, M.C., Shen, H., He, Z., Poirier, G., McCandless, B.E., Livi, K.J., Muller, D.A., Wang, C., Gracias, D.H., 2019. Nano-folded gold catalysts for electroreduction of carbon dioxide. Nano Lett. 19 (12), 9154–9159.
Lei, H., Xing, L., Jiang, H., Wang, Y., Bin Xu, B., Xuan, J., Xiaoteng Liu, T., 2023. Designing graded fuel cell electrodes for proton exchange membrane (PEM) fuel cells with recurrent neural network (RNN) approaches. Chem. Eng. Sci. 267, 118350.
Li, H., Oloman, C., 2007. Development of a continuous reactor for the electro-reduction of carbon dioxide to formate – Part 2: scale-up. J. Appl. Electrochem. 37 (10), 1107–1117.
Liang, S., Altaf, N., Huang, L., Gao, Y., Wang, Q., 2020. Electrolytic cell design for electrochemical CO2 reduction. J. CO2 Util. 35, 90–105.
Lu, X., Leung, D.Y.C., Wang, H., Leung, M.K.H., Xuan, J., 2014. Electrochemical reduction of carbon dioxide to formic acid. ChemElectroChem 1 (5), 836–849.
Ma, S., Sadakiyo, M., Luo, R., Heima, M., Yamauchi, M., Kenis, P.J.A., 2016. One-step electrosynthesis of ethylene and ethanol from CO2 in an alkaline electrolyzer. J. Power Sources 301, 219–228.
Nguyen, T.N., Dinh, C.T., 2020. Gas diffusion electrode design for electrochemical carbon dioxide reduction. Chem. Soc. Rev. 49 (21), 7488–7504.
Ogura, K., 2013. Electrochemical reduction of carbon dioxide to ethylene: mechanistic approach. J. CO2 Util. 1, 43–49.
Palmer, C., Saadi, F., McFarland, E.W., 2018. Technoeconomics of commodity chemical production using sunlight. ACS Sustain. Chem. Eng. 6 (5), 7003–7009.
Pérez-Fortes, M., Schöneberger, J.C., Boulamanti, A., Harrison, G., Tzimas, E., 2016. Formic acid synthesis using CO2 as raw material: techno-economic and environmental evaluation and market potential. Int. J. Hydrog. Energy 41 (37), 16444–16462.
Petrov, K.V., Bui, J.C., Baumgartner, L., Weng, L.C., Dischinger, S.M., Larson, D.M., Miller, D.J., Weber, A.Z., Vermaas, D.A., 2022. Anion-exchange membranes with internal microchannels for water control in CO2 electrolysis. Sustain. Energy Fuels 6, 5077.
Putra, A.S., Sukono, Srigutomo, W., Hidayat, Y., Lesmana, E., 2019. A comparative study of simulated annealing and genetic algorithm method in Bayesian framework to the 2D-gravity data inversion. J. Phys. Conf. Ser. 1204 (1), 012079.
Saves, P.; Lafage, R.; Bartoli, N.; Diouane, Y.; Bussemaker, J.H.; etc., SMT 2.0: a surrogate modeling toolbox with a focus on hierarchical and mixed variables gaussian processes, ArXiv 2023.
Serincan, M.F., Pasaogullari, U., Sammes, N.M., 2009. Effects of operating conditions on the performance of a micro-tubular solid oxide fuel cell (SOFC). J. Power Sources 192 (2), 414–422.

Song, X., Weng, Q., Zhao, Y., Ma, H., Song, J., Su, L., Yuan, J., Liu, Y., 2018. Cloning and expression analysis of ZmERD3 gene from Zea mays. Iran. J. Biotechnol. 16 (2), e1593.
Sumida, B.H., Houston, A.I., McNamara, J.M., Hamilton, W.D., 1990. Genetic algorithms and evolution. J. Theor. Biol. 147 (1), 59–84.
Sun, W., Peppley, B.A., Karan, K., 2005. An improved two-dimensional agglomerate cathode model to study the influence of catalyst layer structural parameters. Electrochim. Acta 50 (16), 3359–3374.
Tan, Y.C., Lee, K.B., Song, H., Oh, J., 2020. Modulating local CO_2 concentration as a general strategy for enhancing C−C coupling in CO_2 electroreduction. Joule 4 (5), 1104–1120.
Wang, H., Leung, D.Y.C., Xuan, J., 2013. Modeling of a microfluidic electrochemical cell for CO2 utilization and fuel production. Appl. Energy 102, 1057–1062.
Wang, J., Jiang, H., Chen, G., Wang, H., Lu, L., Liu, J., Xing, L., 2023. Integration of multi-physics and machine learning-based surrogate modelling approaches for multi--objective optimization of deformed GDL of PEM fuel cells. Energy AI 14, 100261.
Weber, A.Z., Newman, J., 2004. Modeling transport in polymer-electrolyte fuel cells. Chem. Rev. 104 (10), 4679–4726.
Weng, L.C., Bell, A.T., Weber, A.Z., 2018. Modeling gas-diffusion electrodes for CO2 reduction. Phys. Chem. Chem. Phys. 20 (25), 16973–16984.
Weng, L.C., Bell, A.T., Weber, A.Z., 2019a. Towards membrane-electrode assembly systems for CO2 reduction: a modeling study. Energy Environ. Sci. 12 (6), 1950–1968.
Weng, L.C., Bell, A.T., Weber, A.Z., 2020. A systematic analysis of Cu-based membrane–electrode assemblies for CO2 reduction through multiphysics simulation. Energy Environ. Sci. 13 (10), 3592–3606.
Weng, L.C., Bell, A.T., Adam, Z., 2019b. Weber towards, membrane-electrode assembly systems for CO2 reduction: a modeling study. Energy Environ. Sci. 12, 1950–1968.
Whipple, D.T., Kenis, P.J.A., 2010. Prospects of CO2 utilization via direct heterogeneous electrochemical reduction. J. Phys. Chem. Lett. 1 (24), 3451–3458.
Wu, K., Birgersson, E., Kim, B., Kenis, P.J.A., Karimi, I.A., 2015. Modeling and experimental validation of electrochemical reduction of CO2 to CO in a microfluidic cell. J. Electrochem. Soc. 162 (1), F23.
Xiang, H., Rasul, S., Scott, K., Portoles, J., Cumpson, P., Yu, E.H., 2019. Enhanced selectivity of carbonaceous products from electrochemical reduction of CO2 in aqueous media. J. CO2 Util. 30, 214–221.
Xing, L., Jiang, H., Wang, S., Pinfield, V.J., Xuan, J., 2023. Data-driven surrogate modelling and multi-variable optimization of trickle bed and packed bubble column reactors for CO2 capture via enhanced weathering. Chem. Eng. J. 454, 139997.
Xing, L., Song, X.G., Scott, K., Pickert, V., Cao, W., 2013. Multi-variable optimisation of PEMFC cathodes based on surrogate modelling. Int. J. Hydrog. Eng. 38, 14295–14313.
Yamamoto, T., Tryk, D.A., Fujishima, A., Ohata, H., 2002. Production of syngas plus oxygen from CO2 in a gas-diffusion electrode-based electrolytic cell. Electrochim. Acta 47 (20), 3327–3334.
Yang, K., Kas, R., Smith, W.A., Burdyny, T., 2021a. Role of the carbon-based gas diffusion layer on flooding in a gas diffusion electrode cell for electrochemical CO2 reduction. ACS Energy Lett. 6 (1), 33–40.
Yang, Z., Li, D., Xing, L., Xiang, H., Xuan, J., Cheng, S., Yu, E.H., Yang, A., 2021b. Modeling and upscaling analysis of gas diffusion electrode-based electrochemical carbon dioxide reduction systems. ACS Sustain. Chem. Eng. 9 (1), 351–361.
Yang, Z., Li, D., Xing, L., Xiang, H., Xuan, J., Cheng, S., Yu, E.H., Yang, A., 2021c. Modeling and upscaling analysis of gas diffusion electrode-based electrochemical carbon dioxide reduction systems. ACS Sustain. Chem. Eng. 9, 351–361.
Zhang, B., Ye, D.D., Sui, P.C., Djilali, N., Zhu, X., 2014. Computational modeling of air-breathing microfluidic fuel cells with flow-over and flow-through anodes. J. Power Sources 259, 15–24.
Zhao, F., Yao, Z., Luan, J., Song, X., 2016. A novel fused optimization algorithm of genetic algorithm and ant colony optimization. Math. Probl. Eng. 2016, 2167413.